Bulletin of the Seismological Society of America, Vol. 97, No. 2, pp. 417–425, April 2007, doi: 10.1785/0120060061

A Seismoacoustic Analysis of the Gas-Pipeline Explosion near Ghislenghien in Belgium

by Läslo G. Evers, Lars Ceranna, Hein W. Haak, Alexis Le Pichon, and Rod W. Whitaker

Abstract A high-pressure gas pipeline exploded near Ghislenghien in Belgium, on 30 July 2004. Seismic energy of this event was recorded at three nearby seismometers. The origin time of the explosion was determined by analyzing the Rayleigh waves and found to be 06h55m27 ± 2sec coordinated universal time (UTC). Ground truth of the explosion was invoked to assess the accuracy of the location derived from infrasound data recorded over Western Europe. Different infrasonic phases were identified by using array-processing techniques and raytracing through atmospheric models. The analysis showed that the derived location was situated 13 km from the true location. The total area of the uncertainty ellipse, or area to be searched if the source was of unknown origin, was 690 km^2. After the origin time and location, the yield was calculated by comparing infrasonic stratospheric amplitudes with those from a high-explosives dataset and was estimated at 40.9 tons high-explosives equivalent. In summary, this study illustrates the capability of seismic and infrasound data in forensic investigations. Furthermore, the potential of infrasound as a monitoring or verification technique is addressed.

Introduction

Large explosions are known to generate both infrasound and seismic signals. Infrasound is inaudible sound with a lower-frequency cutoff limited by the thickness of the atmosphere or an atmospheric layer. The human hearing threshold of 20 Hz is, in general, taken as upper limit. Examples of the wide variety of explosive sources are nuclear tests (e.g., Posey and Pierce, 1971) and truck bombs (Koper *et al.*, 1999). Le Pichon *et al.* (2002b) and Evers and Haak (2001) reported infrasound from bolides and Ripepe *et al.* (1996) analyzed volcanic signals from Stromboli.

The explosion of a high-pressure gas pipeline occurred near the city of Ghislenghien, Belgium, around 06h57 coordinated universal time (UTC) on 30 July 2004 as reported by the operator Fluxys (personal communication). Ghislenghien is located approximately 40 km southwest of Brussels, Belgium's capital (see Fig. 1). The 1-m-diameter pipe was split in two segments, each reaching approximately 15 km up to the first shutting-down valve. During the ensuing fire, about 2 million m^3 gas were burned until the gas pipes were exhausted. Vegetation was burned in a radius of 200 to 300 m around the event. Flames were reported to reach a height of 200 m, as described by Manders (2004). On a highway situated 500 m from the site, the skin of passing motorists was burned. Nearby cars and buildings were set on fire. Seismic energy was recorded up to a distance of several tens of kilometers while infrasound traveled at least as far as southern Germany. The event resulted in the deaths of 18 people immediately after the explosion.

Recently, the study of infrasound gained renewed interest because of its use as a verification technique for the Comprehensive Nuclear-Test-Ban Treaty (CTBT; see www.ctbto.org). In this context, we study the use of infrasound and seismic measurements to resolve an explosion's characteristics, such as origin time, location, and yield. Furthermore, phase identification of the infrasonic waveforms is achieved by including empirical and actual atmospheric models. Simultaneous observations of infrasonic and seismic energy contribute to forensic investigations of explosions of both known and unknown origin, quantifying the capability of infrasound as a monitoring technique.

Seismic Observations and Origin Time

The explosion was recorded at three nearby short-period seismic stations operated by the Royal Observatory of Belgium (see Fig. 1). In Figure 2 we show the distance versus time relation of stations SKQ, SNF, and BOU. The black line is described by a speed of 346 m/sec, aligning the secondary arrival. This indicates that we are dealing with either an acoustic-infrasound wave or an air-coupled Rayleigh wave (Koper *et al.*, 1999). The particle motion from the one three-component station SKQ was investigated to distinguish between an infrasound and an air–ground-coupled wave. If the wave train shows retrograde particle motion it should be identified as a Rayleigh wave, otherwise longitudinal

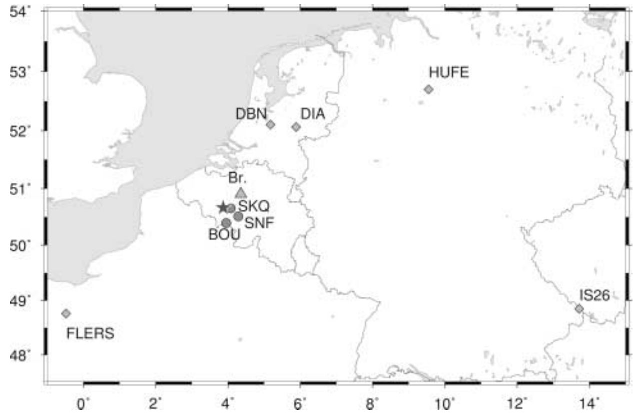

Figure 1. Map of the explosion site and recording instruments. The star gives the position of the explosion in Belgium near the village of Ghislenghien at (3.87° E, 50.66° N), located approximately 40 km southwest of Brussels (triangle). Three short-period seismic stations are located near the explosion site and are denoted by the circles. Furthermore, five diamonds represent the infrasound arrays that recorded energy from the explosion.

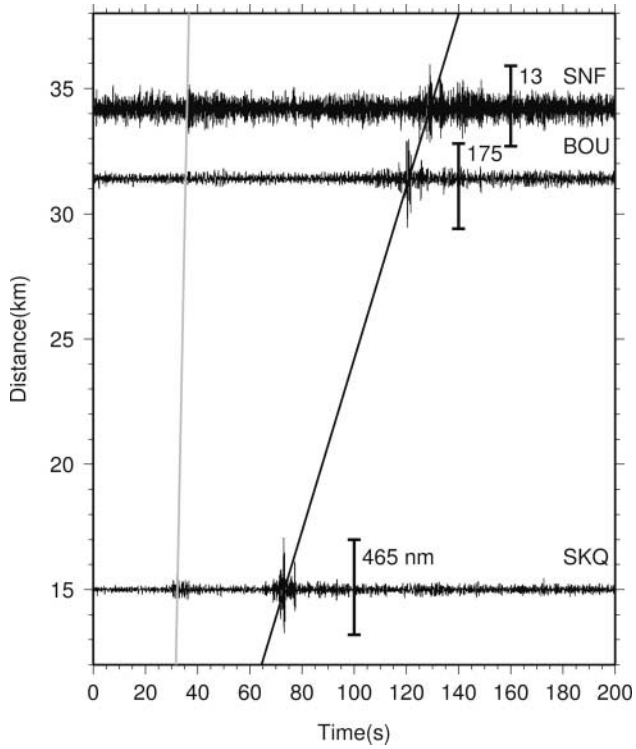

Figure 2. The recordings from the seismic stations in Belgium plotted as epicentral distance versus time graph. The time axis zero time is 06h55m0.0s. The traces of stations SKQ and BOU are bandpass filtered with a second-order Butterworth filter with corner frequencies of 0.5 and 5 Hz. The data from SNF are filtered between 1 and 10 Hz. The peak amplitude of the ground displacement is also given. The black line connects the Rayleigh wave and has a velocity of 346 m/sec. The rather suggestive gray line has a velocity of 5 km/sec and combines a possible *P* wave. The resolved origin time of the explosion is 30 July 2004 06h55m27 ± 2s UTC.

motions would reveal an infrasound wave. The wave appeared to be of a Rayleigh wave nature. The gray line through the first arrival has a velocity of 5 km/sec and might be a *P* wave as a direct seismic wave from the explosion. From Figure 2 it follows that the origin time of the explosion was 06h55m27 ± 2sec UTC. Photographic material shows huge roaring flames during the initial fire. In a personal communication, Fluxys reported that the fire was active until at least 07h45 when small flames were still observed. However, the seismic data do not give any indication of acoustic or seismic waves associated with the fire, as observed by Koper *et al.* (2003). The lack of clear *P* onsets from the explosion makes it difficult to localize the source on the basis of seismic data; most of the energy went into the atmosphere as infrasonic energy.

Infrasound Observations

This event was observed at five infrasound arrays in countries bordering Belgium. In The Netherlands, energy was found at microbarometer arrays in De Bilt (DBN) and in Deelen (DIA) (Evers and Haak, 2003). Infrasound was recorded in France at an array near Flers deployed by the Commissariat à l'Energie Atomique (CEA) (Le Pichon *et al.*, 2002a). In Germany, infrasonic signals were detected at the Bundesanstalt für Grund- und Rohstoffe (BGR), measured by infrasound array IS26 (Hartmann and Henger, 2001), which is part of the International Monitoring System for the CTBT. There was also a temporary array installed north of Hannover in the village of Hufe. The array configurations are given in Figure 3; array apertures range from 60 to 2400 m, while the number of microbarometers varies between 4 and 16.

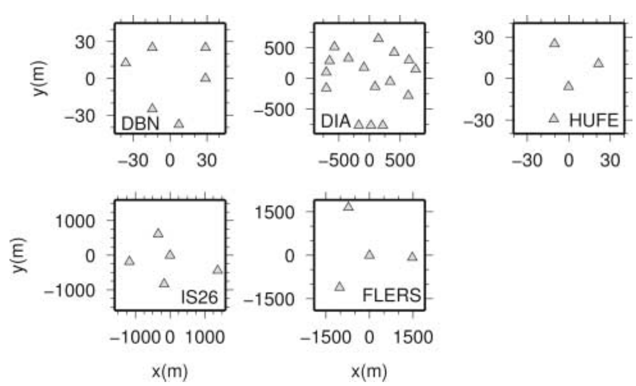

Figure 3. The array layouts of the infrasound stations showing a wide variety in number of microbarometers and apertures.

Signal detection, processing and beamforming were applied based on both the Fisher statistics as described by Melton and Bailey (1957) and the Progressive Multi Channel Cross Correlation (PMCC; Cansi, 1995), which are commonly used in infrasound processing (e.g., Le Pichon *et al.*, 2002a; Evers and Haak, 2003). For these two algorithms, the cross-correlation and Fisher ratio are calculated in the time domain to detect coherent infrasound signals. The time-domain Fisher ratio is given in equation (1).

$$S_f = \frac{T(N-1)}{N(T-1)} \frac{\sum_{t=1}^{T}\left(\sum_{n=1}^{N} X_{nt}\right)^2 - \frac{1}{T}\left(\sum_{t=1}^{T}\sum_{n=1}^{N} X_{nt}\right)^2}{\sum_{t=1}^{T}\sum_{n=1}^{N} X_{nt}^2 - \frac{1}{N}\sum_{t=1}^{T}\left(\sum_{n=1}^{N} X_{nt}\right)^2} \quad (1)$$

Essentially, the variances of N independent observations, the array elements, of quantity X, the air-pressure fluctuations, are evaluated over a timespan T and multiplied by the degrees of freedom. Equation (2) relates the Fisher ratio to the signal-to-noise power ratio (SNR), assuming a plane wave and uncorrelated noise.

$$S_f = 1 + N \cdot \mathrm{SNR} \quad (2)$$

Array-processing techniques like beamforming enable the construction of a best beam, being the sum of all phase-aligned traces in the direction of the source. Figure 4 shows the detection and processing results for the 13 active elements of DIA. A huge increase in Fisher ratio triggers a detection of the infrasound from the initial explosion as visible in the lower frame. A stable backazimuth and apparent sound speed are retrieved through beamforming on a 100 × 100 slowness grid. The best beam and its spectrogram are shown in the top two frames of Figure 4. A coda of infrasound after the initial explosion lasts for at least 15 min, as follows from the high Fisher ratios and a lasting stable backazimuth and apparent sound speed. This coda is caused by roaring flames reaching hundreds of meters into the atmosphere. Table 1 summarizes the characteristics of the infrasound recordings for all arrays based on similar detection and parameter estimation as used for DIA. Infrasound is clearly detected at all arrays; the waveforms, backazimuths, frequency content, and arrival times suggest that we are dealing with infrasound from the explosion. The average backazimuth is calculated by averaging over the complete duration of the signal. Figure 5 shows the best beams for the different arrays as function of the distance. All traces start with an impulsive event, the initial explosion, followed by a coda of infrasound with decreasing amplitude. Except for Flers where clear high-amplitude arrivals are visible throughout the wave train, these are explained in the next section on phase identification. In the most distant arrays, Hufe and IS26, the coda's energy is buried in the noise earlier because of its rather high-frequency content and low amplitude.

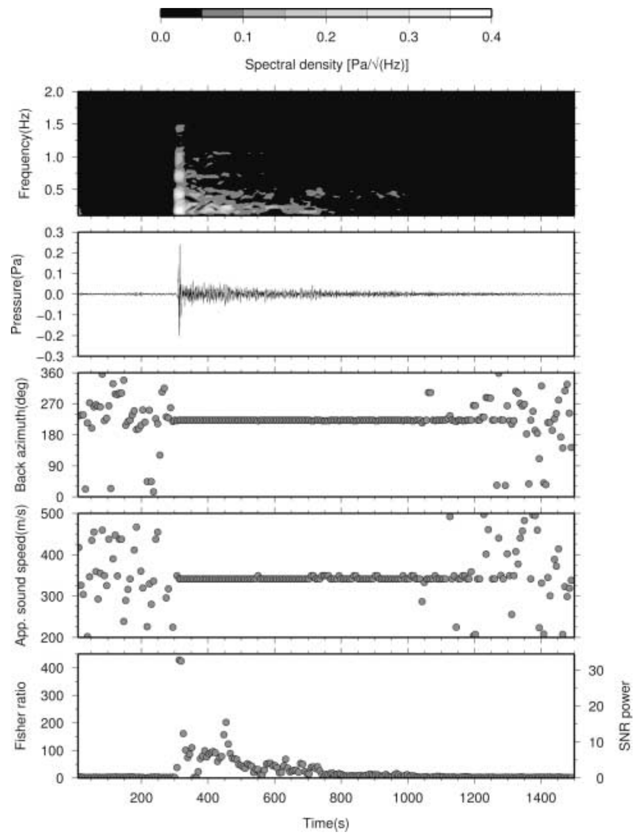

Figure 4. Results of time-domain Fisher ratio analysis on DIA data. The zero time of the horizontal axis is 30 July 2004 07h00m28.2s UTC. The data are filtered with a second-order Butterworth filter with corner frequencies of 0.1 and 10 Hz. Beamforming is done on a 100 × 100 slowness grid, forming 10,000 beams. The data are split in windows of 512 samples (12.8 sec) and processed with a 50% overlap. The lower frame shows the Fisher ratio as function of time and the related (see equation 2) signal-to-noise power ratio. Apparent sound speed and backazimuth are given in the second and third frame, and the best beam is shown in the fourth frame. The top frame shows the spectrogram of the best beam that peaks around 320 sec and 0.2 Hz. The spectrogram is constructed with a sliding window fast Fourier transform (FFT) using 1024 samples with 50% overlap. Table 1 gives the derived event characteristics for all infrasound arrays.

The map on the left of Figure 6 shows the results of cross bearing the derived backazimuths, their uncertainties (in gray), and a star denoting the true location. An ellipse is drawn through the outermost intersection points to confine the total area of interest in case the event was of unknown origin. The cross is the center of the ellipse located at 20 km distance of the source, the total area comprised by the ellipse is 1290 km^2. The uncertainties in this ellipse are given by the accuracy of the determined bearings (in gray). An alternative average location is derived by analyzing each cross-bearing intersection individually. The trigonometric sine is

Table 1
Infrasonic Stations and Observations

	DBN	DIA	Flers	Hufe	IS26
Distance (km)	183.6	208.8	378.6	453.1	737.3
True backazimuth (deg)	210.3	222.9	54.3	242.3	289.6
Arrival time (UTC)	07:04:24.5	07:05:39.0	07:15:27.1 07:17:29.9 07:18:57.6	07:23:19.2	07:43:07.0
Apparent sound speed (m/sec)	354 ± 10	346 ± 5	343 ± 5	328 ± 10	336 ± 5
Backazimuth (deg)	204.3	222.1	53.5	241.3	290.6
Dominant frequency (Hz)	0.2	0.2	0.2	0.2	0.2
Peak amplitude (Pa)	0.8	0.2	0.3	0.2	0.1
Trough amplitude (Pa)	−0.8	−0.2	−0.2	−0.3	−0.1
Duration (sec)	1000	1000	1000	800	500
Average backazimuth (deg)	208.5 ± 0.6	222.1 ± 0.1	53.5 ± 0.1	240.9 ± 1.7	291.8 ± 0.7
Horizontal velocity (km/sec)	I_w: 0.34	I_w: 0.34	I_s: 0.32 I_sI_s: 0.29 I_t: 0.27	I_t: 0.27	I_tI_t: 0.26

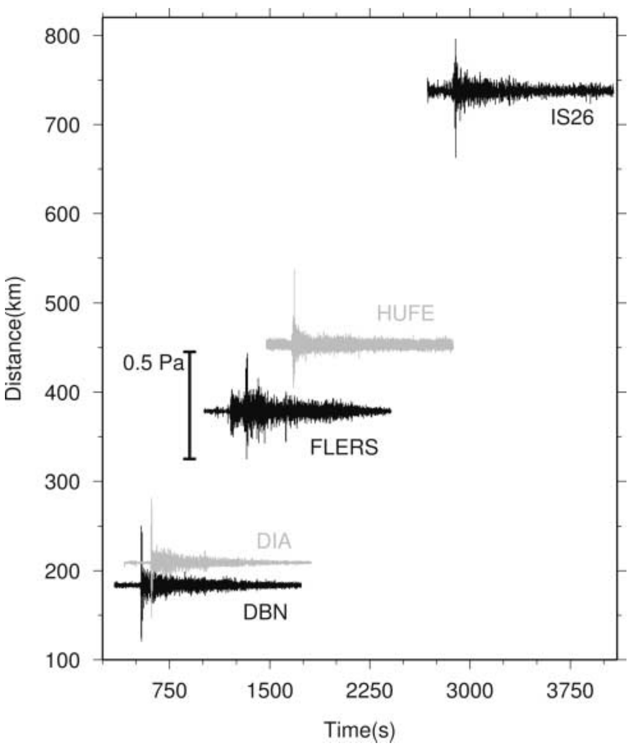

Figure 5. Distance versus time graph of the infrasound data. The time axis zero time is 06u55m27.0s, which is the explosion time as derived from seismic data. The maximum peak and trough amplitudes are indicated and also given in Table 1.

taken from the difference of two bearings and used for weighting the intersection point. The difference of the two bearings ranges between 0 and 90 deg and the associated weights, from taking the sine, between 0 and 1. Doing so, more importance is given to intersection points from more perpendicular bearings that are less sensitive to small errors in one of the bearings. An intersection point from two almost parallel bearings is more unreliable because it can be greatly displaced by small changes in the bearings. The average, called "sine loc" in Figure 6, is the sum of all sine-weighted intersection points divided by the sum of the weights. The atmosphere is a moving medium that causes deviations in the observations, leading to an offset between the true and observed location. This anisotropic nature is partly due to wind, leading to a vectorial translation of the wavefront while traveling through the atmosphere.

Infrasound Propagation through the Atmosphere

In first order, the sound speed is a function of wind and temperature in the atmosphere. The effective sound speed takes both temperature and wind into account by calculating their contributions along the propagation path (see equation 3).

$$v_{\mathrm{eff}} = \sqrt{\gamma r \Theta} + \boldsymbol{n} \cdot \boldsymbol{u} \tag{3}$$

where the multiplication of the ratio of specific heats with the gas constant for air is $\gamma r = 402.8\ \mathrm{m^2\,sec^{-2}\,K^{-1}}$, the absolute temperature is given by θ, and $\boldsymbol{n} \cdot \boldsymbol{u}$ projects the wind $\boldsymbol{u}$ in the direction from source to observer. Atmospheric models were analyzed to account for their influence on the propagation of infrasound. The lower atmosphere up to an elevation of 15 km, that is, the troposphere, is well probed because of its meteorological importance. Details on temperature and wind for the higher atmosphere are less well known. The European Center for Medium Range Weather Forecasting (ECMWF) models the atmosphere up to 65 km within the stratosphere (see www.ecmwf.int). Models for the lower atmosphere are supported by observations from, for example, meteorological balloon measurements. Horizontal Wind Model/Mass Spectrometer and Incoherent Scatter Radar Extended Models (HWM/MSISE) (Hedin *et al.*, 1996), which give the climatology up to a height of 140 km, are used.

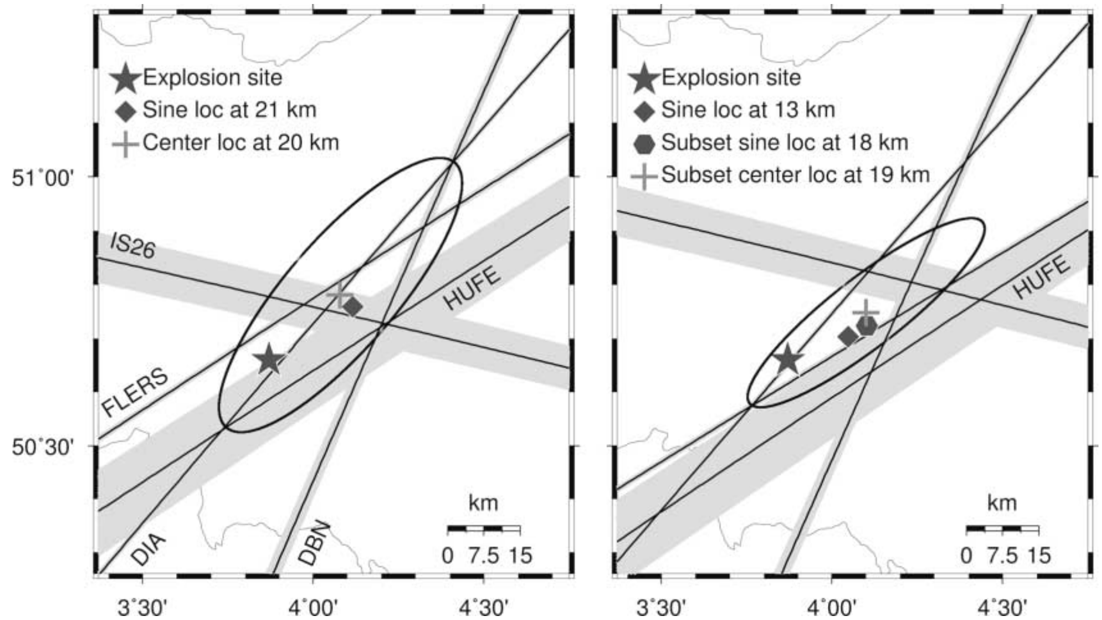

Figure 6. The observed bearings from the infrasound array (left) and the wind corrected bearings (right), see Table 2 for specific values on azimuthal deviations. The gray areas give the standard deviation in back azimuth averaged over the whole signal, see Table 1. The star represents the explosion site, the diamond the average location after sine weighting the cross bearings and the cross is the center of ellipse. The area of uncertainty is 1290 km^2 for raw bearings and 690 km^2 when a subset of wind corrected bearings is used, i.e. Flers, DIA and IS26. The hexagon gives the sine weighted location for the subset.

Depending on the atmospheric wind structure, infrasonic waves may propagate in acoustic wave guides between the ground and troposphere, stratosphere, and lower thermosphere (Brown *et al.*, 2002; Garcés *et al.*, 2004). Multiple arrivals, referred to as phases, may then be recorded at the receiver. They correspond to a specific family of ray paths and turning height levels in the atmosphere, and are characterized by specific values of frequency, amplitude, apparent sound speed, and arrival azimuth along the array beam. Phases associated with waves refracted from the troposphere, referred to as I_w, are strongly dependent on local atmospheric conditions, and may not extend to very long ranges. Considering the short propagation ranges, other phases are unlikely at these stations. Stratospheric phases correspond to infrasonic waves trapped between the stratopause and the ground. These phases, abbreviated as I_s, are dependent on the season of the year and may fluctuate with the passing of storms and other large-scale atmospheric disturbances. They can propagate efficiently for thousands of kilometers. A phase is labeled I_sI_s if the I_s phase has experienced one bounce on the earth's surface. Thermospheric phases correspond to infrasonic waves trapped between the lower thermosphere and the ground. Considering the strong temperature gradient above 90 km, thermospheric paths, abbreviated as I_t, are always predicted. However, due to the low-particle density and nonlinear dissipation in the upper atmosphere, thermospheric returns are strongly attenuated and may not always be observed at large distances (Bass and Sutherland, 2004).

Phase Identification

The horizontal velocity is a useful signal characteristic to identify infrasonic phases and is defined as the epicentral distance divided by the total travel time. Characteristic values for the horizontal velocity are: 0.23–0.28 km/sec for I_t and 0.28–0.31 km/sec for I_s phases (Brown *et al.*, 2002). At DBN and DIA either the direct wave or I_w phase from the explosion is observed, as indicated by the horizontal velocity in Table 1, which equals the sound speed. The I_w phase and direct wave are hard to distinguish based on their horizontal velocity. In Figure 7, multiple arrivals are identified at Flers based on the horizontal velocity, apparent sound speed, and frequency content. Unambiguous phase identification can be achieved by not only taking into account the apparent sound speed but also knowledge of atmospheric winds and temperatures (Garcés *et al.*, 1998). The I_s phase is the first to arrive at Flers followed by the I_sI_s phase. The slight but significant difference in apparent sound speed of 9 m/sec (347 and 338 m/sec) will be explained with raytracing later on. An I_t phase is identified, having the lowest frequency of 0.15 Hz of the whole trace. Further evidence for its thermospheric nature is found in the apparent sound speed of 390 m/sec and the horizontal velocity of 270 m/sec. At Hufe and IS26, stratospheric returns do not exist because the increase of the effective sound speed in the stratopause is not strong enough to refract energy back to the ground. Therefore, I_t and I_tI_t phases are identified at Hufe and

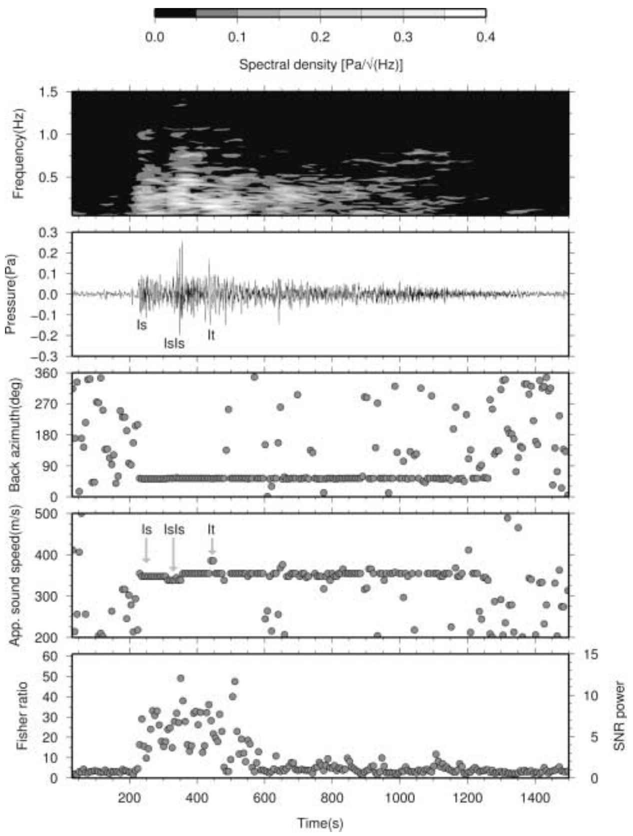

Figure 7. Results of time-domain Fisher ratio analysis on Flers data. The representation is similar to Figure 3. The zero time of the horizontal axis is 30 July 2004 07h11m40.0s UTC. The data are filtered with a second-order Butterworth filter with corner frequencies of 0.05 and 1.5 Hz. The data are split in windows of 256 samples (12.8 sec) and processed with a 50% overlap. Various stratospheric and thermospheric arrivals are indicated.

IS26, respectively, as also follows from the derived horizontal velocities.

We applied the tau-p method as described by Garcés *et al.* (1998) to correct the observed backazimuth for the deviating effects of cross winds along the propagation path and to further identify the phases at Flers. Figure 8 shows an illustration of infrasound propagation from the source toward Flers both through HWM/MSISE (left) and ECMWF (right) models. Both the temperature-dependent sound speed (V_t) and effective sound speed (V_{eff}) are given on the right side of the lower frames. The dashed line represents the effective sound speed at the surface. Energy is refracted from regions where V_{eff} becomes higher than the sound speed at ground level. This is the case in the stratosphere and thermosphere, as described earlier and as follows from the ray trajectories in the lower frames. The middle frames give the travel time for refracted rays within the two models. The top frame shows the locations where rays coincide with the ground, if shot from the source in the direction to the receiver.

The HWM/MSISE model predicts strato- and thermospheric arrivals at Flers, where the thermospheric branch is split into two segments, which represents lower and upper thermospheric refraction regions. The upper and lower branches correspond to a horizontal velocity of 0.26 and 0.29 km/sec, respectively. Compared to the observed horizontal velocity of 0.27 km/sec, the thermospheric phase at Flers is identified as originating from the upper thermosphere. This is further supported by the higher ray density of the upper thermospheric branch. Strong westward zonal cross winds deviate the rays toward the west of Flers as indicated by the negative offsets in the upper frame.

The ECMWF model shows the presence of a tropospheric onset due to a temperature inversion that is hardly visible in the lower frame but clear from the upper two frames, and that fills up first shadow zone with arrivals. An I_s phase reaches Flers and an I_sI_s phase nearly hits Flers but misses by 20 km. This I_sI_s phase is not predicted by the HWM/MSISE model. The I_sI_s phase is predicted by the ECMWF model because the amplitude of the zonal wind is 10 m/sec higher at 60 km height than in the HWM/MSISE model. Underestimating zonal winds might be expected from a climatological model such as HWM/MSISE. Because the I_sI_s phase is identified in the data, we expect only the fastest I_sI_s phase to occur at Flers. This corresponds to the phase with the lowest refraction height in the stratosphere of 40 km. Therefore, the difference in apparent sound speed between the I_s and I_sI_s phase of 9 m/sec is explained by a refraction height of 40 and 50 km, respectively. In the top frame, energy misses Flers and arrives to the west of the station because of stratospheric zonal cross winds. An azimuthal deviation of 1.5 deg is calculated by taking the tangent of the offset and the source–receiver distance. The wind-corrected backazimuths and modeled apparent velocities are given in Table 2 for all arrays, following the same approach as described previously.

The wind-corrected backazimuths are plotted in Figure 6. The decrease in size of the ellipse is clearly noticeable. Here we also discarded the contribution of DBN and Hufe because the apertures of the arrays are too small to correctly characterize an event of 0.2 Hz. The main lobe of the array response is far too broad. With such an aperture precise measurements of backazimuth and apparent sound speed, or slowness, can be obtained for infrasound with a frequency 1.0 Hz and higher. The analysis and modeling of infrasound would lead to search area of 690 km^2 in a similar explosion of unknown origin. This area is described by the ellipse through the relevant outermost intersection points. The various distances between the true and estimated locations range from 13 to 19 km.

Yield of the Explosion

In a personal communication, Fluxys reported a crater diameter of 19 to 20 m and an average depth of 4 m. A relation between crater size and yield was found from nu-

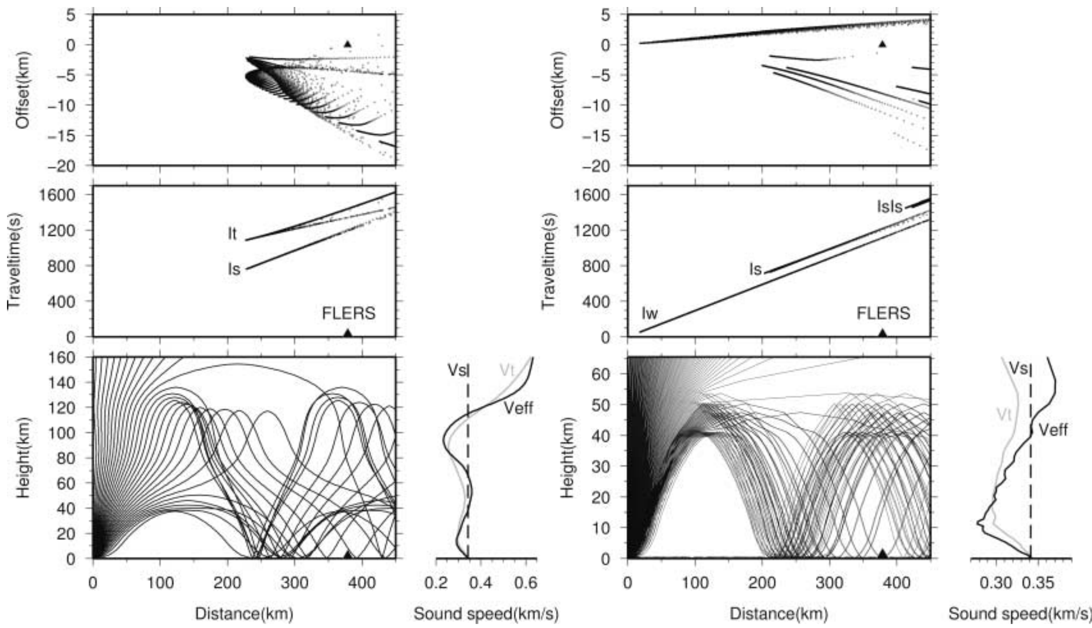

Figure 8. Results from raytracing through HWM (left) and ECMWF (right) models for wind and temperature. The lower frame shows rays leaving the source in the direction of Flers. Rays bend toward the earth's surface between 40 and 55 km height, that is, the stratosphere, and from 120 km upward, that is, the thermosphere. The sound speed is plotted right of the lower frame. The effective sound speed (V_{eff} in black) accounts for both wind and temperature (V_t in gray). Refractions occur from regions where V_{eff} becomes larger than the sound speed at the surface (V_s) as indicated by the dashed line. The middle frame gives the travel time for the rays. The upper frame shows the bounce point of the rays on the Earth's surface. Rays shot from the source [0.0] to Flers [379,0] km are deviated toward the west by zonal cross winds. The azimuthal deviation follows from this representation by taking the tangent of the offset and range.

Table 2
Raytracing Results

	DBN	DIA	Flers			Hufe	IS26
Type of arrival	I_w/direct	I_w/direct	I_s	I_sI_s	I_t	I_t	I_tI_t
Azimuth deviation (deg)	0.5	0.4	1.5	1.0	2.0	−0.6	0.7
Wind-corrected azimuth (deg)	204.8	222.5	55.0	54.5	55.5	240.7	291.3
Travel time (sec)	535	610	1215	1355	1340	1700	2840
Modeled horizontal velocity (km/sec)	0.34	0.34	0.31	0.28	0.26	0.27	0.26

clear tests by Glasstone (1957). The dataset contained depths and diameters of the craters formed by a surface explosion in dry soil with a weapon of energy W in kilotons TNT (ranging from 1 to 20,000 kilotons). The crater diameter scales according to $W^{1/3}$ and the depth according to $W^{1/4}$.

Kinney and Graham (1985) described more precisely the explosive yield W in kilograms TNT as a function of the crater diameter d in meters by equation (4).

$$d = 0.8 W^{1/3} \tag{4}$$

An estimate of the explosive yield is 14.5 tons TNT using an average value of 19.5 m for the crater diameter. Equation (4) is based on data from 200 large surface explosions.

An alternative approach is tested by using the high explosives (HE) dataset from Los Alamos National Laboratory. A relation between infrasonic stratospheric amplitude and charge weight has been derived from this dataset. The high explosive shots cover charge weights of ~20 to 4880 tons observed at stations varying in distance from 250 to 5330 km. The range R in kilometers is scaled as shown in equation (5.1) with the charge weight in kilotons of high explosives.

$$SR = \frac{R}{\sqrt{2 \times chgwt}} \tag{5.1}$$

Furthermore, the amplitudes of observed stratospheric arrivals are wind corrected, using the wind speed at 50 km altitude in the direction of propagation. Equation (5.2) shows the projection of the meridional and zonal wind in meters per second, in the direction from source to observing station, as also used for calculating the effective sound speed.

$$V_d = -(V_z \sin(\theta) + V_m \cos(\theta)) \qquad (5.2)$$

The observed raw amplitudes, peak-to-peak in microbars, are wind corrected with the empirical relation given in equation (5.3).

$$\log(P_{\text{wca}}) = \log(P_{\text{raw}}) - 0.018\, V_d \qquad (5.3)$$

The sense of the wind correction is to normalize to a zero wind condition. Thus if one is in favorable wind propagation, the normalized amplitude would be less than the observed. In the Northern Hemisphere summer, a source west of the receiver is favorable because the receiver is downwind of the source due to westward stratospheric zonal winds. Figure 9 gives the wind-corrected stratospheric amplitude as function of the scaled range for high explosives. The line is formed by the regression relation given as equation (5.4).

$$P_{\text{wca}} = 5.95 \times 10^{04} (SR)^{-1.4072} \qquad (5.4)$$

ANFO stands for ammonium nitrate fuel oil, a widely used explosive, data points are given by the circles (see Fig. 9). The triangles relate to the Watusi test, a high-explosives experiment done at the Nevada test site in the United States during 2002. Flers is the only station where clear stratospheric arrivals could be identified and is, therefore, the only station for which this empirical relation can be applied. Here, we use the regression relation in an inverse manner. Based on the observed amplitude we calculate the charge weight. The amplitude of 0.5 Pa, corresponding to the initial explosion, is wind corrected to 0.2 Pa with a zonal wind of −39.3 m/sec (east–west) and meridional wind of −6.2 m/sec (north–south) from ECMWF model at 50 km altitude. The wind-corrected amplitude is fitted to the regression curve as shown by the square in Figure 9. From the scaled range a charge weight of 40.9 tons high explosives is calculated.

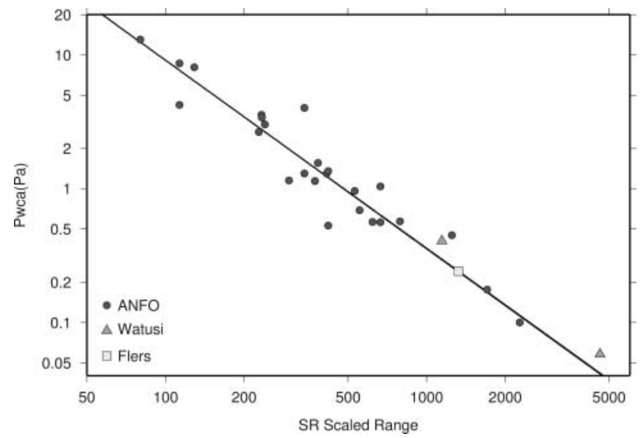

Figure 9. The Watusi and ANFO data from Los Alamos National Laboratory, displayed as wind-corrected peak amplitude versus scaled range. The wind-corrected amplitude of Flers is fitted to the curve resolving a charge weight of 40.9 tons of high explosives equivalent.

Discussion and Conclusions

The explosion of a high-pressure gas pipeline near Ghislenghien, Belgium, generated both seismic and acoustic or infrasound signals. The seismic signals, recorded at nearby seismometers, revealed an origin time of 06h55m27 ± 2sec UTC on 30 July 2004 based on the arrival times of Rayleigh waves.

Infrasound traveled over Western Europe and was recorded as far as southern Germany, at a distance of 738 km. Other recording infrasound arrays were located in France and The Netherlands. Several phases were observed due to the broad epicentral coverage of infrasound arrays. These phases were identified by using their horizontal velocities, apparent sound speed, and frequency contents, and by ray-tracing through both climatological and event-specfic atmospheric models. The arrays in The Netherlands recorded direct or tropospheric refracted phases, I_w. In France both stratospheric, I_s, and thermospheric, I_t, phases were identified. Even an I_sI_s phase was extracted from the data corresponding to waves having one bounce on the earth's surface coming from the stratosphere. The German arrays received energy refracted in the thermosphere: I_t and I_tI_t phases.

The source was located, as being of unknown origin, by correcting the observed backazimuths for winds and discarding incompetent small arrays. Comparing the results to the ground truth location, it was found that the source location could be confined up to a distance of 13 km leaving a search area of 690 km^2 by using wind-corrected bearings. This quantifies the capability and accuracy of infrasound as monitoring technique for this specific event.

The strength of the source was determined by comparing the observed stratospheric amplitude in France to the high-explosives (HE) dataset of Los Alamos National Laboratory. The HE dataset contains wind-corrected stratospheric amplitudes of a wide variety of ranges and yields. A yield of 40.9 tons HE yield equivalent was derived by fitting the wind-corrected amplitude from the Flers station to the regression curve of the HE dataset. Although, the yield derived from the crater size is of the same order of the magnitude, that is, 14.5 tons TNT, the unknown source mechanisms make this value unreliable. Gas was smelt prior to explosion; therefore, the explosion might well be the result of the ignition of an area of gas-saturated soil. Rather than being a confined explosion at one point, this source should be regarded as distributed over an area. To estimate the yield from the crater size, as having a point source, is in this case less applicable.

In conclusion, the seismoacoustic analysis of an explosion can reveal the origin time, location, and yield of the explosion. To accurately reach this goal, infrasonic phases should be interpreted based on array-processing techniques and the use of climatological and event-specific atmospheric models. The use of broadband arrays, in terms of frequency, enhances the detection and location capability for a large range of possible explosion sizes and locations.

Acknowledgments

The Royal Netherlands Airforce is thanked for their cooperation in DIA. We acknowledge the contribution of seismic data by the Royal Observatory of Belgium. The help of Marc Allaart, KNMI, with obtaining ECMWF's atmospheric data is appreciated. Figures in this article were made with the Generic Mapping Tool described in Wessel and Smith (1991).

References

Bass, H. E., and L. C. Sutherland (2004). Atmospheric absorption in the atmosphere up to 160 km, *J. Acoust. Soc. Am.* **115,** 1012–1032.

Brown, D. J., C. N. Katz, R. Le Bras, M. P. Flanagan, J. Wang, and A. K. Gault (2002). Infrasonic signal detection and source location at the Prototype Data Centre, *Pure Appl. Geophys.* **159,** 1081–1125.

Cansi, Y. (1995). An automatic seismic event processing for detection and location: the P.M.C.C. Method, *Geophys. Res. Lett.* **22,** 1021–1024.

Evers, L. G., and H. W. Haak (2001). Listening to sounds from an exploding meteor and oceanic waves, *Geophys. Res. Lett.* **28,** 41–44, doi 10.1029/2000GL011859.

Evers, L. G., and H. W. Haak (2003). Tracing a meteoric trajectory with infrasound, *Geophys. Res. Lett.* **30,** 2246, doi 10.1029/2003GL017947.

Garcés, M., D. P. Drob, and J. M. Picone (2002). A theoretical study of the effect of geomagnetic fluctuations and solar tides on the propagation of infrasonic waves in the upper atmosphere, *Geophys. J. Int.* **148,** 77–87.

Garcés, M. A., R. A. Hansen, and K. G. Lindquist (1998). Traveltimes for infrasonic waves propagating in a stratified atmosphere, *Geophys. J. Int.* **135,** 255–263.

Garcés, M., M. Willis, C. Hetzer, A. Le Pichon, and D. Drob (2004). On using ocean swells for continuous infrasonic measurements of winds and temperature in the lower, middle, and upper atmosphere, *Geophys. Res. Lett.* **31,** L19304, doi 10.1029/2004GRL020696.

Glasstone, S. (1957). *The Effect of Nuclear Weapons*, U.S. Atomic Energy Commission, Washington, D.C., 196–227.

Hartmann, G., and M. Henger (2001). Milestones of IS26 Installation, paper presented at the Infrasound Workshop, Passau, Germany, 2–6 October.

Hedin, A. E., E. L. Fleming, A. H. Manson, F. J. Schmidlin, S. K. Avery, R. R. Clark, S. J. Franke, G. J. Fraser, T. Tsuda, F. Vial, and R. A. Vincent (1996). Empirical wind model for the upper, middle and lower atmosphere, *J. Atmos. Terr. Phys.* **58,** 1421–1447.

Kinney, G. F., and K. J. Graham (1985). *Explosive Shocks in Air*, Springer-Verlag, New York, 9–10.

Koper, K. D., T. C. Wallace, and R. C. Aster (2003). Seismic recordings of the Carlsbad, New Mexico, pipeline explosion of 19 August 2000, *Bull. Seism. Soc. Am.* **93,** 1427–1432.

Koper, K. D., T. C. Wallace, and D. Hollnack (1999). Seismic analysis of the 7 August 1998 truckbomb blast at the American Embassy in Nairobi, Kenya, *Seism. Res. Lett.* **70,** 512–521.

Le Pichon, A., M. Garcés, E. Blanc, M. Barthélémy, and D. P. Drob (2002a). Acoustic propagation and atmosphere characteristics derived from infrasonic waves generated by the Concorde, *J. Acoust. Soc. Am.* **111,** 629–641.

Le Pichon, A., J. M. Guérin, E. Blanc, and D. Reymond (2002b). Trail in the atmosphere of the 29 December 2000 meteor as recorded in Tahiti: Characteristics and trajectory reconstruction, *J. Geophys. Res.* **107,** 4709, doi 10.1029/2001JD001283.

Manders, B. (2004). Major gas pipe explodes at 80 bar, killing eighteen, in *Offshore News Letter*, Fugro Robertson BV, Netherlands Offshore Information Services, The Netherlands, 3–4.

Melton, B. S., and L. F. Bailey (1957). Multiple signal correlators, *Geophysics* **22,** 565–588.

Posey, J. W., and A. D. Pierce (1971). Estimation of nuclear explosion energies from microbarograph records, *Nature* **232,** 253.

Ripepe, M., P. Poggi, T. Braun, and E. Gordeev (1996). Infrasonic waves and volcanic tremor at Stromboli, *Geophys. Res. Lett.* **23,** 181–184.

Wessel, P., and W.H.F. Smith (1991). Free software helps map and display data, *EOS Trans. AGU* **72,** 441.

Royal Netherlands Meteorological Institute
Seismology Division
P.O. Box 201
3730 AE De Bilt, The Netherlands
evers@knmi.nl, haak@knmi.nl
(L.G.E, H.W.H.)

Bundesanstalt für Geowissenschaften und Rohstoffe
Stilleweg 2
D-30655 Hannover, Germany
ceranna@sdac.hannover.bgr.de
(L.C.)

Commissariat à l'Energie Atomique
B.P. 12
91680 Bruyeres-Le-Chatel, France
alexis.le-pichon@cea.fr
(A.L.P.)

Los Alamos National Laboratory
P.O. Box 1663
Los Alamos, New Mexico 87545
rww@lanl.gov
(R.W.W.)

Manuscript received 18 March 2006.